CARDIFF UNIVERSITY
PRIFYSGOL CAERDYDD

ORCA – Online Research @ Cardiff

This is an Open Access document downloaded from ORCA, Cardiff University's institutional repository:https://orca.cardiff.ac.uk/id/eprint/87099/

This is the author's version of a work that was submitted to / accepted for publication.

Citation for final published version:

Kondrat, Simon A., Smith, Paul J., Wells, Peter P., Chater, Philip A., Carter, James H., Morgan, David J. , Fiordaliso, Elisabetta M., Wagner, Jakob B., Davies, Thomas E., Lu, Li, Bartley, Jonathan K. , Taylor, Stuart H. , Spencer, Michael S., Kiely, Christopher J. , Kelly, Gordon J., Park, Colin W., Rosseinsky, Matthew J. and Hutchings, Graham J. 2016. Stable amorphous georgeite as a precursor to a high-activity catalyst . Nature 531 , pp. 83-87. 10.1038/nature16935

Publishers page: http://dx.doi.org/10.1038/nature16935

Please note:
Changes made as a result of publishing processes such as copy-editing, formatting and page numbers may not be reflected in this version. For the definitive version of this publication, please refer to the published source. You are advised to consult the publisher's version if you wish to cite this paper.

This version is being made available in accordance with publisher policies. See http://orca.cf.ac.uk/policies.html for usage policies. Copyright and moral rights for publications made available in ORCA are retained by the copyright holders.

Stable amorphous georgeite as a precursor to a high activity catalyst

Simon A. Kondrat[1*], Paul J. Smith[1], Peter P. Wells[2,3], Philip A. Chater[4,5], James H. Carter[1], David J. Morgan[1], Elisabetta M. Fiordaliso[6], Jakob B. Wagner[6], Thomas E. Davies[1,5], Li Lu[7], Jonathan K. Bartley[1], Stuart H. Taylor[1], Michael S. Spencer[1], Christopher J. Kiely[7], Gordon J. Kelly[8], Colin W. Park[8], Matthew J. Rosseinsky[5] and Graham J. Hutchings[1*]

[1] Cardiff Catalysis Institute, School of Chemistry, Cardiff University, Main Building, Park Place, Cardiff, CF10 3AT, U.K.

[2] The UK Catalysis Hub, Research Complex at Harwell, Harwell, Oxon, OX11 0FA, U.K.

[3] Kathleen Lonsdale Building, Department of Chemistry, University College London, Gordon Street, London, WC1H 0AJ, U.K.

[4] Diamond Light Source, Didcot, OX11 0DE, U.K.

[5] Department of Chemistry, University of Liverpool, Crown Street, Liverpool, L69 7ZD, U.K.

[6] Center for Electron Nanoscopy, Technical University of Denmark, Fysikvej 307, DK-2800 Kgs. Lyngby, Denmark

[7] Department of Materials Science and Engineering, Lehigh University, 5 East Packer Avenue, Bethlehem, PA 18015, U.S.A.

[8] Johnson Matthey, PO Box 1, Belasis Avenue, Cleveland, TS23 1LB, U.K.

*Hutch@cardiff.ac.uk and KondratSA@cardiff.ac.uk

Copper and zinc form an important group of hydroxycarbonate minerals that include zincian malachite, aurichalcite and rosasite. Georgeite also belongs to this mineral family but little is known about it, due to its exceptional rarity, low purity, instability and highly disordered nature. Zincian malachite[1,2], aurichalcite[3] and rosasite[1,2] are catalyst precursors for methanol synthesis and the low temperature water-gas shift (LTS) reaction, which are important for the production of chemical intermediates[4-6]. Precursor phases strongly influences the activity of the final catalyst with zincian malachite being the desired phase[1,2,7-9]. Its preparation by co-precipitation involves the transient formation of amorphous georgeite[10], which then transforms rapidly to crystalline malachite. This method often, but not exclusively[11E], uses Na_2CO_3 that introduces Na^+, which can be a poison for catalysis. The inability to synthesise stable georgeite, or even to find mineralogical examples of georgeite with high purity, has led to it being largely ignored[12]. We have previously shown that well-mixed copper manganese oxides can be prepared by supercritical anti-solvent (SAS) precipitation using CO_2.[13] The high diffusion rates and solvation power of supercritical carbon dioxide ($scCO_2$) used in SAS, rapidly expand and supersaturate solutions, leading to highly disordered materials; we considered that this approach could be adapted to synthesise copper zinc hydroxycarbonate precursors with low Na^+ content. Here we show that stable georgeite can be synthesised using $scCO_2$as an anti-solvent in a precipitation process[14]. This synthetic georgeite is a precursor to highly active methanol synthesis and LTS catalysts that display in the latter case superior stability to comparable catalysts prepared from crystalline malachite.

We investigated the SAS process using copper(II) acetate solutions, with the precipitates being characterised by XRD and FT-IR (Extended data Figure 1) . The use of ethanol as solvent produced amorphous copper(II) acetate. Addition of 5vol% water as a co-solvent produced a blue precipitate with an IR spectrum exhibiting a broad -OH band at 3408 cm^{-1}. This IR signature is very different from malachite and closely matches the spectrum used to identify the rare georgeite phase[10]. As with mineralogical georgeite, the phase produced was amorphous by XRD. ICP-MS and CHN analysis (Extended data Figure 2) gave an ideal formula of $Cu_7(CO_3)_5(OH)_4.5H_2O$, with helium pycnometry giving a density of 3.1 g cm^{-3} for the SAS-prepared georgeite . Slight variations in composition are anticipated for an amorphous phase[15], and hence we consider that the CHN analysis closely matches the $Cu_5(CO_3)_3(OH)_4.6H_2O$ formula reported for georgeite[10] . The SAS-prepared and mineralogical forms of georgeite both have a higher CO_3^{2-}/Cu^{2+} molar ratio than malachite (with CO_3^{2-}/Cu^{2+} values of 0.7, 0.6 and 0.5 respectively). This differs from previous studies that asserted georgeite and malachite ($Cu_2CO_3(OH)_2$) were iso-compositional[16], as georgeite rapidly transformed into malachite. Such instability was not observed for SAS-prepared georgeite, as the rapid solvent extraction produced georgeite that was effectively dry from the point of precipitation. This limits contact with water, which

facilitates the ageing process and transformation to malachite. Next we investigated the SAS precipitation of mixed copper and zinc acetate (2:1 and 1:1 Cu:Zn) solutions, which formed zincian-georgeite (having 2:1 or 1:1 Cu:Zn ratio by ICP) with a near identical density (Extended data Figure 2), IR spectrum and XRD pattern (Extended data Figure 1) to that of copper-only georgeite, with no additional phases, *e.g.* smithsonite ($ZnCO_3$), discernible by XRD. STEM analysis (Extended data Figure 3) of zincian georgeite (analysis of georgeite not possible due to its instability under vacuum) predominantly showed amorphous material, although a small volume fraction (<10 vol%) of sub-2nm CuO_x crystallites were observed. In addition, the SAS-derived zincian georgeite has few impurities (*e.g.* Na^+ ions) present, (Extended data Figure 2).

It was therefore possible to synthesise stable zincian georgeite by SAS in sufficient quantities to allow further exploration of its properties. The catalytic performance of Cu/ZnO, derived from zincian georgeite, for the methanol synthesis and LTS reactions was evaluated. For comparative purposes a zincian-malachite precursor was synthesised by co-precipitation (see methods) as this is considered the optimal precursor for model Cu/ZnO catalysts[2]. Catalysts used in this study were not stabilised with alumina, an important promoter and stabiliser of the commercial catalyst[17,18]. Prior to use, the precursors were calcined to remove the carbonate followed by *in-situ* reduction to form the active catalyst. Thermal gravimetric analysis (TGA) with evolved gas analysis (EGA) was performed (Figure 1) to determine the optimal calcination temperature. SAS-prepared georgeite has a significantly different mass loss profile to malachite, with georgeite exhibiting three distinct mass losses and malachite a single mass drop loss associated with concurrent removal of H_2O and CO_2. The multi-step decomposition of georgeite and zincian-georgeite (1:1 Cu:Zn sample shown in Extended data Figure 2) can be separated into three regions: H_2O loss at 80-100°C, H_2O and CO_2 loss at 190-210°C and CO_2 alone at 315-420°C (carbonate decomposition). Based on the TGA analysis the precursors were calcined at 300°C in air for 6h, as this is below the temperature associated with CO_2 evolution and residual carbonate species have been shown to improve the activity of methanol synthesis catalysts[19]. The calcined material was then reduced *in-situ* in dilute hydrogen at 225°C.

The activity of these model catalysts (Figure 2) was contrasted with that of commercial catalysts. For both reactions the catalyst derived from SAS-prepared zincian-georgeite was more active than those formed from zincian-malachite and the standard commercial catalyst, although the enhancement in activity observed for methanol synthesis, with its significantly higher Cu surface area normalised initial productivity (Extended data Figure 4), was short lived. However, for the LTS reaction the SAS-prepared zincian-georgeite derived catalyst was far more active and stable over the entire test period. Indeed, the enhanced activity was apparent at all contact times investigated (Figure 2). The availability of

stable zincian-georgeite as a precursor gives access to highly active copper-zinc oxide catalysts. This LTS activity and stability can be maintained with 50% less Cu when using a catalyst derived from a 1:1 Cu:Zn georgeite (Extended data Figure 4).

We decided to probe the structure of georgeite to understand the origins of the enhanced activity. Due to the stability and large quantities of SAS georgeite produced, we were able to apply a range of advanced characterisation techniques and make comparisons to known phases. X-ray absorption near-edge structure (XANES) data for Cu-only georgeite and malachite precursors (Figure 3a) indicates that both materials have Cu present as Cu^{2+} in a distorted octahedral environment,[20] in agreement with diffuse reflectance UV-Vis spectroscopy (DRS) and extended X-ray absorption fine structure (EXAFS) data (Figure 3 b, Extended data Table 1). However, both UV-Vis and XANES analysis suggests subtle differences in coordination geometries exist between georgeite and malachite. The optical band associated with metal centre(s) in georgeite was located at 770 nm in DRS, whereas the combined bands from the two crystallographic Cu centres in malachite occur at 825 nm[21].

Although XANES data for georgeite and malachite are similar, there are clear differences in the EXAFS. The Fourier transform of the EXAFS χ data (Figure 3b) show clear differences at larger R (>2Å), with malachite having contributions further out, correlated to the scattering effects of Cu-Cu neighbours. Conversely the georgeite EXAFS data has very few features beyond 2Å and no evidence of metal-metal correlation. The addition of Zn did not affect metal geometry in georgeite with no discernible changes in the Cu EXAFS data or Zn K-edge XANES or EXAFS χ-plots of zincian georgeite, indicating no evidence of impurity phases such as $ZnCO_3$ (Extended data Figure 5).

X-ray pair distribution function (PDF) analysis, which does not suffer from scattering path phasing phenomena, was used to further probe the short-to-medium range order. The PDFs of georgeite and zincian-georgeite have strikingly similar strong short-range order (up to 5Å) (Figure 3d); with subtle differences between 5 and 10Å and less long-range order in the georgeite. The extended order observed by Zn addition could be responsible for the enhanced stability of zincian-georgeite prepared by co-precipitation[16]. A comparison of the georgeite PDF with a calculated PDF of malachite[22] (Figure 3e) shows that georgeite is not simply a nano-scale form of malachite, as noted for other amorphous minerals such as FeS[23]. The complete absence of the 15.27Å correlation between crystallographically identical Cu atoms in georgeite shows local ordering operates well below the length-scales associated with the malachite unit cell. PDF matching to other copper phases such as aurichalcite[24], azurite[25] and rosasite[26] confirmed that georgeite was a distinct material from any known copper hydroxycarbonate (Extended data Figure 5).

The development of the final Cu/ZnO catalyst involves the 300 °C calcination of zincian-georgeite and malachite precursors to form CuO/ZnO intermediates, followed by reduction to form the active phase. We now show that the final state catalysts exhibit a chemical memory of their precursors and calcined intermediates, as the microstructure of materials produced on calcination and reduction reflect the structural characteristics of their precursor phase.

Calcination of SAS prepared zincian-georgeite produced disordered 3-4 nm nanocrystalline CuO/ZnO as observed by STEM and PDF analysis (Extended data Figure 6 and 7). The extent of the disorder resulted in XRD and XANES analysis showing no discernible metal oxide contribution, although subtle changes in the EXAFS were observed (Extended data Figure 8). Disordered CuO species have been previously reported to have Cu edge XANES data that fit with a Jahn-Teller distorted octahedron, as with the calcined zincian georgeite[27]. This nanocrystallinity was found to persist until the residual high temperature carbonate decomposes to form XRD discernible CuO and ZnO phases above 425°C. (Extended data Figure 7) Conversely, calcination of zincian malachite at temperatures greater than 300°C produced crystalline, XRD and XANES observable, CuO and ZnO phases (Extended data Figure 7). A linear combination fit of the XANES data showed that 60% of the 300°C calcined zincian malachite (Extended data Figure 8) was associated with CuO and ZnO, whereas these phases were not present in the calcined zincian-georgeite. STEM showed that 300 °C calcined zincian-malachite (Extended data Figure 6) was comprised of CuO and ZnO grains with much longer range crystalline order than the corresponding calcined zincian-georgeite.

The nanocrystalline nature of calcined zincian-georgeite translates to a high Cu surface area ($53 m^2 g^{-1}$) and small mean Cu crystallite size (7.4±0.7nm) when the material is reduced. Environmental transmission electron microscopy (ETEM) carried out under reducing conditions shows a complex mixture of Cu particles and exceptionally small disordered ZnO grains (2.8±1.6nm mean ZnO crystallite size by XRD), with significant Cu-ZnO interaction (Figure 4). By comparison, the more crystalline zincian-malachite derived CuO/ZnO had a lower Cu surface area ($35 m^2 g^{-1}$) and a microstructure comprised of discrete larger Cu (mean crystallite size of 14.2±3.8nm by XRD) and ZnO (mean crystallite size of 5.6±3.6nm by XRD) particles. This difference in Cu and ZnO particle size and structural order is reflected in the smaller Cu-Cu and Zn-Zn coordination numbers, noted for the zincian-georgeite derived catalyst from *in-situ* EXAFS analysis (Extended data Figure 9). On a macroscopic level strong Cu-ZnO metal support interaction, as evidenced by XPS observations of partial ZnO_x coverage of Cu on reduction[7], was observed for both catalysts (Extended data Figure 9). However, ETEM shows considerably more Cu-ZnO interface present in the catalyst derived from disordered zincian-georgeite.

Methanol synthesis activity is well known to strongly correlate with copper surface area[28]. In addition, high Cu-ZnO interfacial area has previously been reported to produce highly active methanol synthesis catalysts[29], with the active site associated with surface defect Cu-sites decorated by Zn[7]. Under 40h of LTS conditions copper surface areas were shown to decrease markedly for both zincian-georgeite (53± $3m^2g^{-1}$ to $17±1m^2g^{-1}$) and zincian-malachite ($38±2m^2g^{-1}$ to $19±1m^2g^{-1}$) derived catalysts. Clearly initial Cu surface areas do not adequately correlate with activity of the catalysts. The combination of higher exposed Cu content and intimate interface contact between Cu and ZnO, inherited from the zincian-georgeite precursor, provides an explanation for the high activity of this catalyst. The SAS method produces very pure zincian-georgeite with low Na^+ ion content that does not require an aqueous washing step. This high purity could also be a contributing factor to both the high activity and stability of the zincian-georgeite derived LTS catalyst.

Acknowledgements

We would like to thank Catherine Brooks, Leon Van de Water, Helen Stanness and Colin Ramson for technical assistance. In addition we acknowledge, e Johnson Matthey and EPSRC for funding though a CASE award, UK Technology Strategy Board and the EPSRC and UK Catalysis Hub (EP/K014714/1, EP/K014714/1, EP/K014668/1, EP/K014706/1, EP/I019693/1) for funding. We would like to acknowledge the use of the Diamond light source for access to B18 (allocation number SP8071) with D. Gianolio and G. Cibin help and beamline I15 that contributed to the PDF results. This research used resources of the Advanced Photon Source, a U.S. Department of Energy (DOE) Office of Science User Facility operated for the DOE Office of Science by Argonne National Laboratory under Contract No. DE-AC02-06CH11357. We thank Karena Chapman for the collection of PDF data at beamline 11-ID-B, APS. The A.P. Møller and Chastine Mc-Kinney Møller Foundation is gratefully acknowledged for their contribution toward the establishment of the Center for Electron Nanoscopy in the Technical University of Denmark. Source data are available at http://dx.doi.org/10.17035/d.2015.0008102108

Author contributions

SK, JB, ST, MS, GK, CP, MR, CK and GH designed the experiments. SK and PS carried out the sample preparation TGA/EGA analysis and IR spectroscopy; SK, PS and JC carried out the catalysis evaluation and Cu surface area determinations; SK, PS and PC carried out the XRD analysis; PC carried out the PDF analysis; PW, SK and PS carried out the XAFS and interpretation; LL and CK carried out the TEM and interpretation; EF, JW, CK and SK carried out the ETEM and interpretation; DM, PS and SK carried out the XPS and the interpretation. CK, JW, GK, MR and GH were involved in the writing and

editing of the manuscript. GH directed the research. Correspondence and requests for materials should be addressed to GH hutch@cf.ac.uk.

References

1 Spencer, M. S. The role of zinc oxide in Cu/ZnO catalysts for methanol synthesis and the water-gas shift reaction. *Top. Catal.* **8**, 259-266 (1999).

2 Behrens, M. Meso- and nano-structuring of industrial Cu/ZnO/(Al_2O_3) catalysts. *J. Catal.* **267**, 24-29, doi:10.1016/j.jcat.2009.07.009 (2009).

3 Fujitani, T. & Nakamura, J. The effect of ZnO in methanol synthesis catalysts on Cu dispersion and the specific activity. *Catal. Lett.* **56**, 119-124 (1998).

4 Chinchen, G. C., Denny, P. J., Jennings, J. R., Spencer, M. S. & Waugh, K. C. Synthesis of methanol. Part 1. Catalysts and kinetics. *Appl. Catal.* **36**, 1-65, doi:10.1016/S0166-9834(00)80103-7 (1988).

5 Rhodes, C., Hutchings, G. J. & Ward, A. M. Water-gas shift reaction: finding the mechanistic boundary. *Catal. Today* **23**, 43-58, doi:10.1016/0920-5861(94)00135-O (1995).

6 Short, G. D., Chinchen, G. C. & Williamson, J. G., Synthesis of methanol; finely divided oxides of zinc, aluminum, magnesium; with metallic copper, US4788175 (1988).

7 Behrens, M. *et al.* The active site of methanol synthesis over Cu/ZnO/Al_2O_3 Iindustrial catalysts. *Science (Washington, DC, U. S.)* **336**, 893-897, doi:10.1126/science.1219831 (2012).

8 Baltes, C., Vukojevic, S. & Schueth, F. Correlations between synthesis, precursor, and catalyst structure and activity of a large set of CuO/ZnO/Al_2O_3 catalysts for methanol synthesis. *J. Catal.* **258**, 334-344, doi:10.1016/j.jcat.2008.07.004 (2008).

9 Bems, B. *et al.* Relations between synthesis and microstructural properties of copper/zinc hydroxycarbonates. *Chem. - Eur. J.* **9**, 2039-2052, doi:10.1002/chem.200204122 (2003).

10 Bridge, P. J., Just, J. & Hey, M. H. Georgeite, a new amorphous copper carbonate from the Carr Boyd Mine, Western Australia. *Mineral. Mag.* **43**, 97-98, doi:10.1180/minmag.1979.043.325.04 (1979).

11 Prieto, G., de Jong, K. P. & de Jongh, P. E. Towards 'greener' catalyst manufacture: Reduction of wastewater from the preparation of Cu/ZnO/Al_2O_3 methanol synthesis catalysts. *Catal. Today* **215**, 142-151, doi:10.1016/j.cattod.2013.03.033 (2013).

12 Pollard, A. M. *et al.* Georgeite and azurite as precursors in the preparation of coprecipitated copper/zinc oxide catalysts. *Appl. Catal., A* **85**, 1-11, doi:10.1016/0926-860X(92)80125-V (1992).

13 Tang, Z.-R. *et al.* New Nanocrystalline Cu/MnO_x catalysts prepared from supercritical antisolvent precipitation. *Chem.Cat.Chem* **1**, 247-251, doi:10.1002/cctc.200900195 (2009).

14 Reverchon, E. Supercritical antisolvent precipitation of micro- and nano-particles. *J. Supercrit. Fluids* **15**, 1-21, doi:10.1016/S0896-8446(98)00129-6 (1999).

15 Rogers, A. P. A review of the amorphous minerals. *J. Geol.* **25**, 515-541, doi:10.1086/622518 (1917).

16 Pollard, A. M., Thomas, R. G., Williams, P. A., Just, J. & Bridge, P. J. The synthesis and composition of georgeite and its reactions to form other secondary copper(II) carbonates. *Mineral. Mag.* **55**, 163-166, doi:10.1180/minmag.1991.055.379.03 (1991).

17 Behrens, M. *et al.* Performance Improvement of nanocatalysts by promoter-Induced defects in the support material: methanol synthesis over Cu/ZnO:Al. *J. Am. Chem. Soc.* **135**, 6061-6068, doi:10.1021/ja310456f (2013).

18 Campbell, J. S. Influences of catalyst formulation and poisoning on the activity and die-off of low temperature shift catalysts. *Ind. Eng. Chem., Process Des. Develop.* **9**, 588-595, doi:10.1021/i260036a016 (1970).

19 Schur, M. *et al.* Continuous coprecipitation of catalysts in a micromixer: Nanostructured Cu/ZnO composite for the synthesis of methanol. *Angew. Chem. Int. Ed.* **42**, 3815-3817, doi:10.1002/anie.200250709 (2003).

20 Rothe, J., Hormes, J., Bonnemann, H., Brijoux, W. & Siepen, K. In situ X-ray absorption spectroscopy investigation during the formation of colloidal copper. *Journal of the American Chemical Society* **120**, 6019-6023, doi:10.1021/ja972748w (1998).

21 Klokishner, S. *et al.* Cation Ordering in Natural and Synthetic $(Cu_{1-x}Zn_x)_2CO_3(OH)_2$ and $(Cu_{1-x}Zn_x)_5(CO_3)_2(OH)_6$. *J. Phys. Chem. A* **115**, 9954-9968, doi:10.1021/jp205848s (2011).

22 Behrens, M. & Girgsdies, F. Structural Effects of Cu/Zn Substitution in the Malachite-Rosasite System. *Zeitschrift Fur Anorganische Und Allgemeine Chemie* **636**, 919-927, doi:10.1002/zaac.201000028 (2010).

23 Michel, F. M. *et al.* Short- to medium-range atomic order and crystallite size of the initial FeS precipitate from pair distribution function analysis. *Chemistry of Materials* **17**, 6246-6255, doi:10.1021/cm050886b (2005).

24 Harding, M. M., Kariuki, B. M., Cernik, R. & Cressey, G. The structure of aurichalcite, $(CuZn)_5(OH)_6(CO_3)_2$ detremined from a microscrystal. *Acta Crystallographica Section B-Structural Science* **50**, 673-676, doi:10.1107/s0108768194007470 (1994).

25 Belokoneva, E. L., Gubina, Y. K. & Forsyth, J. B. The charge density distribution and antiferromagnetic properties of azurite $Cu_3[CO_3]_2(OH)_2$. *Phys. Chem. Miner.* **28**, 498-507, doi:10.1007/s002690100176 (2001).

26 Perchiazzi, N. & Merlino, S. The malachite-rosasite group: crystal structures of glaukosphaerite and pokrovskite. *Eur. J. Mineral.* **18**, 787-792, doi:10.1127/0935-1221/2006/0018-0787 (2006).

27 Belin, S. *et al.* $CuAu/SiO_2$ catalysts for the selective oxidation of propene to acrolein: the impact of catalyst preparation variables on material structure and catalytic performance. *Catal. Sci. Technol.* **3**, 2944-2957, doi:10.1039/c3cy00254c (2013).

28 Chinchen, G. C., Waugh, K. C. & Whan, D. A. The activity and state of the copper surface in methanol synthesis catalysts. *Appl. Catal.* **25**, 101-107, doi:10.1016/s0166-9834(00)81226-9 (1986).

29 Behrens, M. *et al.* The Potential of Microstructural Optimization in Metal/Oxide Catalysts: higher Intrinsic Activity of Copper by Partial Embedding of Copper Nanoparticles. *ChemCatChem* **2**, 816-818, doi:10.1002/cctc.201000017 (2010).

Figures captions

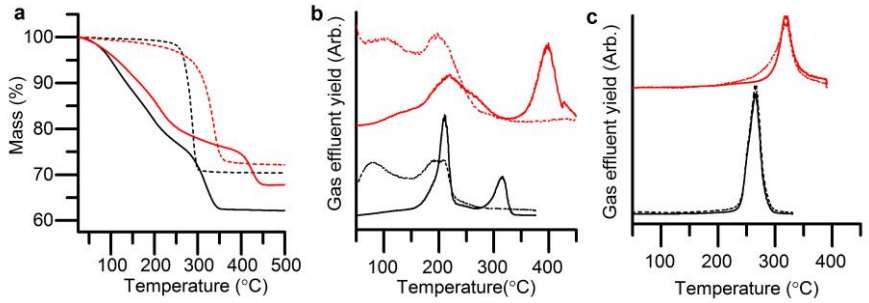

Figure 1. Thermal gravimetric analysis (TGA) with evolved gas analysis (EGA) of georgeite and malachite. (a) TGA of georgeite (black solid line), zincian georgeite (red solid line), malachite (black dotted line) and zincian malachite (red dotted line). (b) EGA of georgeite (black lines) and zincian georgeite (red lines). (c) EGA of malachite (black lines) and zincian malachite (red lines). In both (b) and (c), the solid lines indicate CO_2 (mass 44 fragment) and dashed lines H_2O (mass 18 fragment).

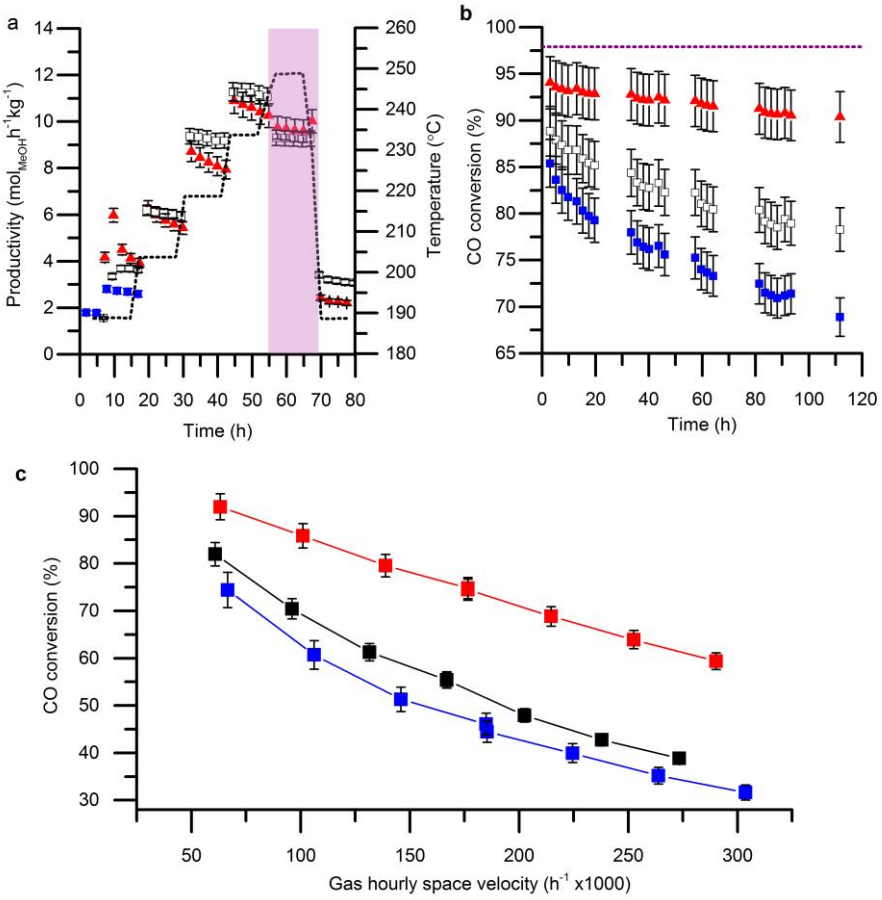

Figure 2. Catalyst test results: (a) Mass normalised time-on-line methanol productivity; (b) CO conversion for LTS reaction time-on-line ((...) represents maximum equilibrium conversion); (c) LTS conversions at different gas-hourly-space-velocities. LTS mass normalised data, Cu mass normalised productivities/activities, initial Cu surface area normalised productivities/activities and product impurities are shown in Extended data figure 4. *Key*: (---) shows representative methanol synthesis reactor bed temperature; (▲) zincian georgeite derived catalyst; (■) co-precipitated zincian malachite derived catalyst (□) industrial standards (methanol synthesis catalyst composition by wt% is

$CuO:ZnO:Al_2O_3$ = 60:30:10, LTS catalyst composition by wt% is $CuO:ZnO:Al_2O_3$ = 50:33:17). *Reaction conditions for methanol synthesis:* 190-250 °C (shaded area shows reaction under equilibrium conditions at 250°C), 25 bar, gas composition $CO:CO_2:H_2:N_2$ = 6:9.2:67:17.8, MHSV = 7200 $Lkg^{-1}h^{-1}$. All selectivities to methanol >99.96%. *Reaction conditions for LTS*: 220°C, 27.5bar, gas composition $H_2O:CO:CO_2:H_2:N_2$ = 50:2:8:27.5:12.5, MHSV = 75000 $Lkg^{-1}h^{-1}$.

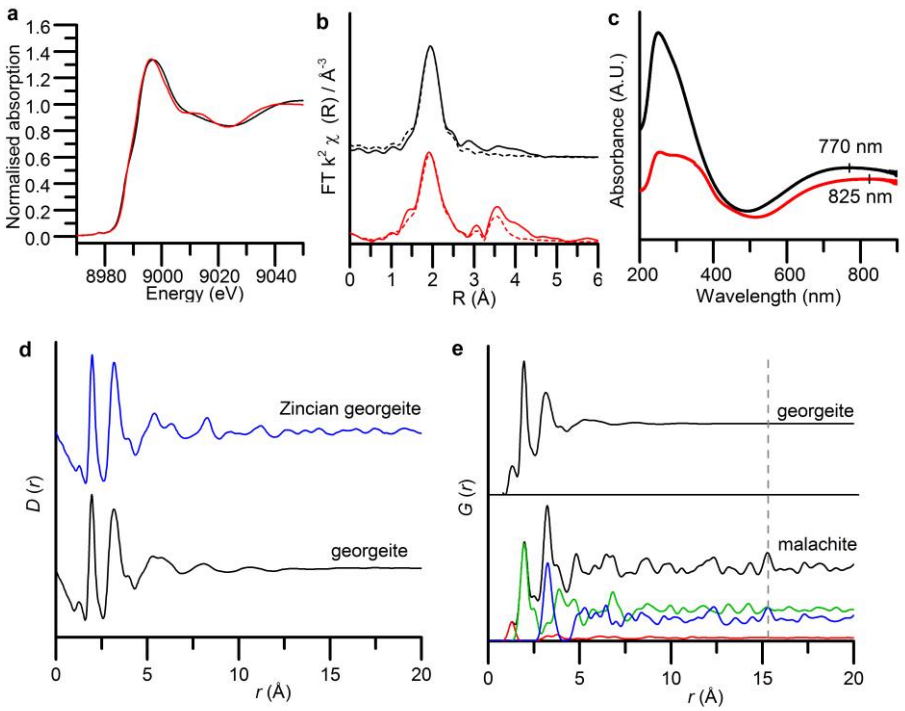

Figure 3. **X-ray adsorption fine edge spectroscopy (XAFS) and X-ray pair distribution function (PDF) analysis**. (a) Cu K-edge XAFS information on local structure; malachite (red line), georgeite (black line). (b) Fourier transform of extended X-ray adsorption fine edge spectra (EXAFS) using fitting parameters for malachite and georgeite. The fit was modelled on 4 shorter Cu-O bond distances and 2 longer Jahn-Teller distorted Cu-O bond distances (Extended data table 1). (c) UV-vis spectra with centres of d-d transition bands marked; malachite (red line), georgeite (black line) (zincian phases in Extended data figure 5a). (d) Comparison of X-ray PDF data for georgeite and zincian georgeite. (e) i) Observed PDF *G*(*r*) data of georgeite. ii) Calculated PDF data of malachite, together with the partial contributions from the most strongly contributing atom pairs; C–O (red), Cu–O (green) and Cu–Cu (blue). Dotted line represents a contribution from crystallographically equivalent Cu atoms.

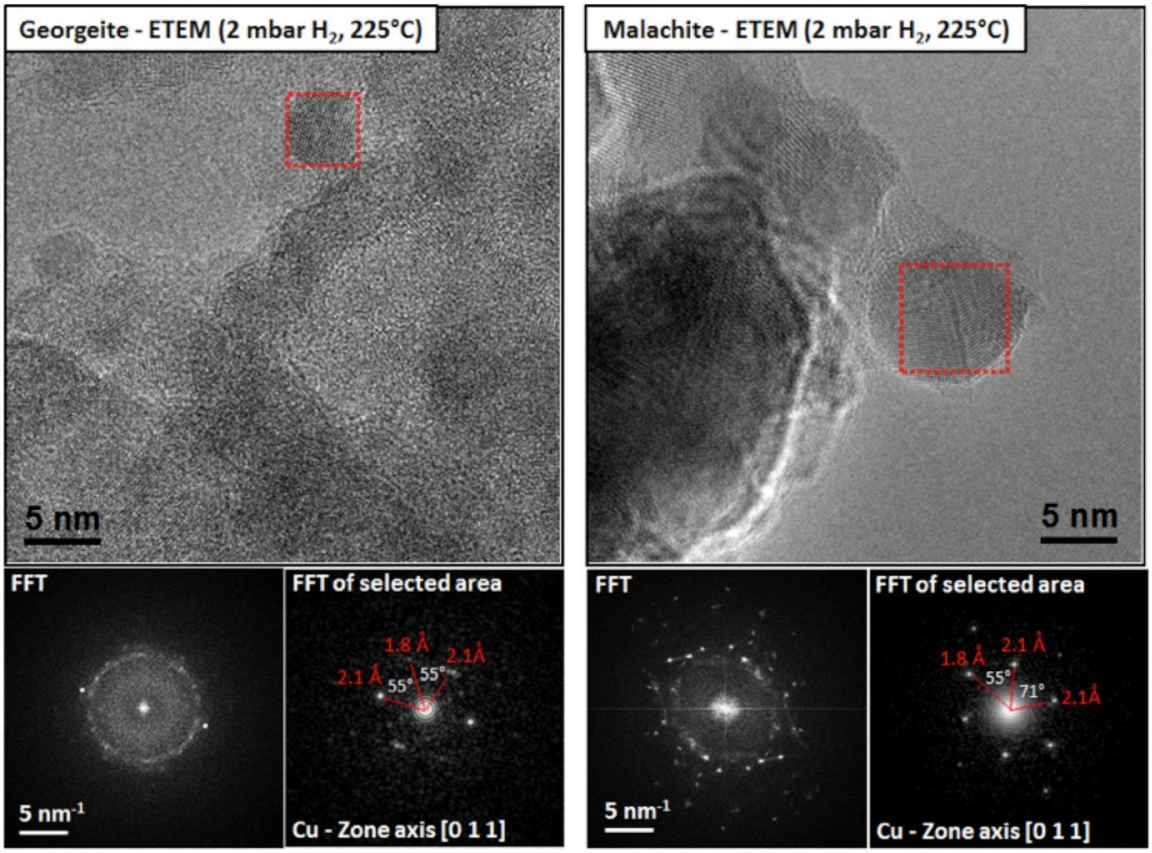

Figure 4. Microstructure of the reduced georgeite and malachite precursors characterized by ETEM in 2mbar H_2 at 225˚C. Both samples reveal distinct Cu nanoparticles distributed on ZnO as confirmed by FFT analysis. The reduced malachite sample generally has larger Cu nanoparticles compared to the georgeite sample. A substantially greater Cu-ZnO interaction exists in the georgeite-derived sample compared to the malachite-derived catalyst during *in -situ* reduction. The georgeite sample has a complex mix of Cu and poorly defined ZnO (as revealed by diffuse rings in the large scale FFTs) compared to the better defined phase-separated Cu and ZnO within the malachite-derived catalyst. The oxidation state of Cu was monitored by means of EELS (Extended data 10) which revealed that Cu was in its metallic state for both samples under the *in-situ* reduction conditions.

Extended Data Figure 1| FT-IR and XRD characterisation of SAS Cu and Cu/Zn acetate precipitates. Sample key: (i) SAS prepared copper acetate,(ii) SAS prepared georgeite, (iii) malachite prepared by co-precipitation, (iv) 2:1 Cu:Zn malachite prepared by co-precipitation, (v) SAS prepared 2:1 Cu:Zn georgeite, (vi) SAS prepared 1:1 Cu:Zn georgeite, (vii) SAS prepared zmithsonite ($ZnCO_3$). **a**, XRD analysis of Cu only samples. **b**, FT-IR of Cu only samples. **c**, FT-IR band assignment of Cu only samples with (ref) designates as received copper (II) acetate monohydrate. * The presence of this band shows that SAS precipitation with no additional water co-solvent produced some georgeite as well as amorphous copper acetate. We attribute the formation of georgeite to the small amount of water present from the monohydrated starting salt. **d,** IR spectrum of mineralogical georgeite, reproduced with the permission of the Mineralogical Society of Great Britain and Ireland from Bridge et al.[10].**e,** FT-IR spectra of Cu:Zn samples. **f**, XRD of Cu:Zn samples.

Extended Data Figure 2| Composition of and Cu and Cu:Zn samples with supplementary TGA analysis. a, Elemental composition of SAS georgeite and co-precipitated malachite samples. Elemental composition was determined by CHN analysis and ICP-MS. Densities were determined by helium pycnometry.[a] Values from reference 10. .[b] Values from reference 16 . * Density determined by sink-float (SF) method. Helium pycnometry used in the current study provides a skeletal density that negates buoyancy effects. **b**, Comparison of experimental and calculated mass losses for georgeite

and malachite from TGA measurements. * Calculated from assumption of final products being 2:1 CuO:ZnO. The lower than expected mass losses for the zincian phases could be associated with Cu^{2+} inclusion in the ZnO lattice. **c**, TGA analysis of 2:1 Cu:Zn georgeite (red line) and 1:1 Cu:Zn georgeite (black line).

Extended Data Figure 3| Representative (a) DF-STEM and (b) BF-STEM micrographs of the zincian georgeite precursor. The general morphology of the zincian georgeite precursor is shown the DF-STEM micrograph presented in Figure 5S(a). It typically consists of very characteristic irregularly shaped agglomerates, about 100-200nm in diameter, of 'amorphous' ~40nm scale non-facetted particles. Closer inspection by BF-STEM, as presented in Figure 5S(b), shows that these latter particles consist of an amorphous matrix phase in which are embedded largely disconnected sub-2nm crystallites of ordered material exhibiting clear lattice fringes. The amorphous matrix, probably containing the carbonate and hydroxyl species, is by far the majority phase, while the nanocrystallites make up less than 10% by volume of the material. This observation is consistent with our other characterization data as signals from the matrix phase would dominate the XAFS analysis, whereas the nanocrystallites are too small in dimension to be detected by XRD. Analysis of fringe spacings and interplanar angles from individual nanocrystallites from such images suggest that some of the grains could be CuO (tenorite, where the Cu is 4-fold co-ordinated by O), while others fit better to Cu_2O (cuprite, where the Cu has a coordination number of is 2). No convincing lattice fringe matches to either ZnO, or $ZnCO_3$ could be found.

Extended Data Figure 4| Additional Catalytic testing for methanol synthesis reaction and LTS reaction. ▲2:1 Cu:Zn georgeite, △1:1 Cu:Zn georgeite, ☐ industrial standard and ■ 2:1 Cu:Zn malachite (this test was terminated after 190 °C temperature stage, due to poor activity). Methanol synthesis data normalised to total mass (**a**) and Cu mass (**b**), at 190 to 250 ° C. (--) shows representative reactor bed temperature. *Reaction conditions:* temperature shown by dashed line, 25 bar pressure, gas composition $CO:CO_2:H_2:N_2$ = 6:9.2:67:17.8, MHSV = 7200 L kg^{-1} h^{-1}. **c,** Concentration of the by-products from the methanol synthesis reaction collected in the condensate pot after reaction. Concentrations determined by GC analysis. Comparison of catalyst activities for LTS reaction normalised to total catalyst mass (**d**) and Cu mass (**e**). *Reaction conditions:* temperature 220 °C, 27.5 bar pressure, gas composition $H_2O:CO:CO_2:H_2:N_2$ =50:2:8:27.35:12.5, MHSV= 75000 l kg^{-1} h^{-1}.**f,** Concentration of the methanol collected in the condensate pot after LTS reaction. Concentrations determined by GC analysis. **g,** Table of methanol synthesis productivities and LTS activities normalised by copper surface area. * Copper surface area analysis determined by N_2O reactive frontal chromatography prior to testing. § Methanol synthesis data acquired at 190 °C with steady state being at 18 h time on line. ^ LTS data acquired at 220 °C with steady state being at 40 h time on line. It is important to note that LTS simulation testing showed that copper surface area dropped significantly after 40 h (17 and 19 m^2g^{-1} for zincian georgeite and zincian malachite derived catalysts respectively). The inverse correlation between copper surface area and initial productivity also suggests that loss of surface area rapidly occurs during reaction and therefore initial rate data is likely to be inaccurate.

Extended Data Table 1| EXAFS fitting parameters for georgeite and malachite. *Fitting parameters for malachite:* S_0^2 = 0.72 as deduced by CuO standard; Fit range 3<k<12, 1<R<3.5; # of independent points = 14. *Fitting parameters for georgeite:* S_0^2 = 0.72 as deduced by CuO standard; Fit range 3<k<12, 1<R<3.5; # of independent points = 14

Extended Data Figure 5| Spectroscopic analysis of the addition of Zn to georgeite. a, Diffuse reflectance UV-vis spectra of zincian malachite (red) and zincian georgeite (black). **b,** Cu K edge EXAFS (χ) comparison of zincian georgeite with georgeite. **c,** Zn K edge XANES comparison of zincian georgeite (4:1 and 2:1 Cu:Zn ratios) with SAS prepared smithsonite. **d,** Zn K edge EXAFS (χ) comparison of zincian georgeite (4:1 and 2:1 Cu:Zn ratios) with SAS prepared smithsonite. **e**, Comparison of observed

georgeite PDF data with simulated data for crystalline hydroxyl carbonate minerals with similar compositions to georgeite; namely aurichalcite, azurite, rosasite, zincian malachite and malachite.

Extended Data Figure 6| Representative DF-STEM and BF-STEM micrographs of 300 °C calcined zincian georgeite and zincian malachite. a, DF-STEM of calcined zincian georgeite. Higher magnification imaging (Fig. S18(b)) reveals that after the loss of much of the carbonate and hydroxyl content has been driven off by the calcination treatment, the majority of the disordered matrix material originally present in the precursor has now crystallized and only a very small amount of amorphous material remains. Interestingly the crystallized material is entirely in a nanocrystalline form, with a mean grain diameter of 3-4nm, which is just below the detection limit for XRD. Analysis of the fringe spacings and interplanar angles from individual grains suggests the material is now mainly an intimate mixture of zinc and copper oxides and the small amount of disordered material detected corresponds to the residual occluded carbonate material as detected by TGA/EGA analysis on this material. **b,** BF-STEM of calcined zincian georgeite. **c,** DF-STEM of calcined zincian malachite. **d,** BF-STEM of calcined zincian malachite.

Extended Data Figure 7| X-ray diffraction analysis of calcined zincian georgeite and zincian malachite. a, PDF of zincian georgeite and after calcination at 120°C, 200°C, 250°C, 300°C and 450°C. There is little change in the observed PDF up to 250°C other than a slight peak broadening, which can be attributed to a reduction in short-range order. The dashed line shows the position of the C–O peak, which is retained until above 300°C. **b** PDF and **C,** Rietveld fits of zincian georgeite after calcination at 450°C. The measured data is shown as open circles, the fit is a solid black line and the difference is a grey line. Both techniques determine the product to be a mixture of CuO and ZnO (weight ratio of 68:32 by PDF; 67.7(4):32.3(4) by Rietveld). **d,** *Ex-situ* XRD patterns following calcination of zincian georgeite for 2 h at: (i) 250 °C; (ii) 300 °C; (iii) 450 °C. Key: (○) CuO; (■) ZnO. **e,f,** *In-situ* XRD analysis of zincian georgeite (**d**) and zincian malachite (**e)** samples during calcination between 300 and 500 °C under an atmosphere of static air, with XRD scans every 25 °C.

Extended Data Figure 8| Cu K edge XAFS analysis of 300 °C calcined zincian georgeite and zincian malachite. a, EXAFS (χ) comparison of CuO, calcined zincian georgeite and calcined zincian georgeite. **b,** EXAFS (R) comparison of CuO (green), calcined zincian georgeite (black) and calcined zincian georgeite (blue). **c-e,** Linear combination fit of CuO and ZnO with zincian malachite calcined at 300 °C.

Extended Data Figure 9| In-situ characterisation of final state reduced Cu/ZnO catalysts derived from 300 °C calcined zincian georgeite and zincian malachite. **a,** XRD of zincian georgeite derived catalyst after *in-situ* hydrogen reduction (2% H_2/N_2 at 225 °C for 1 h). Fine dotted lines indicate ZnO reflections and dashed lines metallic Cu. **b**, Cu K edge EXAFS FT of final reduced catalysts derived from zincian georgeite and zincian malachite. **c**, Cu K edge EXAFS fit of reduced catalyst catalysts. **d**, Zn K edge EXAFS FT of final reduced catalysts derived from zincian georgeite and zincian malachite. **e**, Zn K edge EXAFS fit of reduced catalyst catalysts**. f**, Electron Energy-Loss spectra (EELS) of georgeite and malachite sample, respectively during reduction in the ETEM experiment. The EELS spectra were acquired in 2 mbar H_2 at 225˚C. showing the fine structure of the Cu $L_{2,3}$ ionization edges characteristic for metallic Cu^0. **g**, EXAFS fitting data for Cu and Zn K edge data. Fitting parameters for K edge Cu: S_0^2 = 0.91 as deduced by cu foil standard; Fit range 3<k<11.2, 1<R<5.5; # of independent points = 23;*denotes multiple scattering path. Fitting parameters for K edge Zn: S_0^2 = 0.90 as deduced from a ZnO_2 standard; Fit range 3.3<k<9.5, 1<R<4.8; # of independent points = 16;*denotes multiple scattering path. **h**, XPS analysis of calcined and reduced catalysts derived from zincian georgeite and zincian malachite.

Methods

Material preparation

Supercritical anti-solvent precipitation method for the preparation of georgeite and zincian georgeite

Copper(II) acetate monohydrate (4 mg ml^{-1}) and zinc(II) acetate dehydrate (2.16 mg ml^{-1}) (Sigma Aldrich ≥99% Puriss), were dissolved in ethanol (reagent grade, Fischer Scientific) containing 0, 5 or 10 vol% deionized water. Smithsonite $ZnCO_3$ was prepared with zinc(II) acetate dehydrate (2.16 mg ml^{-1}) in a 10 vol% water and ethanol solution. Supercritical anti-solvent (SAS) experiments were performed using apparatus manufactured by Separex. CO_2 (BOC) was pumped through the system (held at 110 bar, 40 °C) *via* the outer part of a co-axial nozzle at a rate of 6 kg h^{-1}. The metal salt solution was concurrently pumped through the inner nozzle, using an Agilent HPLC pump at a rate of 6.4 ml min^{-1}. The resulting precipitate was recovered on a stainless steel frit, while the CO_2-solvent mixture passed down stream, where the pressure was decreased to separate the solvent and CO_2. The precipitation vessel has an internal volume of 1L. Precipitation was carried out for 120 min followed by a purge of the system with ethanol-CO_2 for 15 min then CO_2 for 60 min under 110 bar and 40 °C. The system was then depressurised and the dry powder collected. Recovered samples were placed in a vacuum oven at 40 °C for 4 h to remove any residual solvent. Approximately 1.5 g of georgeite is prepared during the 120 min duration of solution precipitation.

Co-precipitation method for the preparation of malachite and zincian malachite

The preparation of standard methanol synthesis catalysts was performed employing a semi-continuous process using two peristaltic pumps to maintain pH. Copper(II) nitrate hydrate and zinc(II) nitrate hydrate solutions in de-ionised water were prepared with Cu:Zn molar ratios of 1:0, 1:1 and 2:1. The pre-mixed metal solution (5 L, ~ 0.5 g ml^{-1}) was pre-heated along with a separate 5 L solution of 1.5 M sodium carbonate. The mixed metals were precipitated by combining the two solutions concurrently at 65 °C, with the pH being held between 6.5 and 6.8. The precipitate would spill over from the small precipitation pot into a stirred ageing vessel, held at 65 °C. The precipitate was aged for 15 min after all precursor solutions had been used.

The precipitate was than filtered and washed to minimise sodium content. The sample was washed with 6 L of hot de-ionised water and the sodium content monitored using a photometer. The washing process was repeated until the sodium content showed no change. The sample was then dried at 110 °C for 16 h. Samples were calcined for 6 h at 300 or 450 °C in a tube furnace under static air. The ramp rate used to reach the desired temperature was 10 °C min^{-1}.

Catalyst testing

Catalyst testing was performed with 0.5 g of the calcined catalyst, pelleted and ground to a sieve fraction 0.6-1 mm for both the methanol synthesis and low temperature water-gas shift test reactions. The catalysts were reduced *in-situ* using a 2% H_2/N_2 gas mixture at 225 °C (ramp rate of 1 °C min^{-1}), prior to the reaction gases being introduced.

Methanol synthesis

Testing was performed in a single stream six-fixed bed reactor with an additional by-pass line. After reduction the catalysts were then subjected to synthesised syngas ($CO:CO_2:H_2:N_2$ = 6.9:2:67:17.8) at 3.5 l h^{-1}, 25 bar pressure and 195 °C. In-line gas analysis was performed using an FT-IR spectrometer, which detected CO, CO_2, H_2O and CH_3OH. Downstream of the catalyst beds, knockout pots collected effluent produced from the reaction. The contents were collected after each test run and analysed using gas chromatography to evaluate the selectivity of catalysts. The total system flow was maintained using the by-pass line.

Low-temperature water-gas shift

Testing was performed in six parallel fixed bed reactors with a single stream feed and an additional by-pass line. After reduction the catalysts were subjected to synthetic syngas ($CO:CO_2:H_2:N_2$ = 1:4:13.75:6.25) at 27.5 bar pressure and 220 °C. The reactant gas stream was passed though vaporised water to give a water composition of 50 vol%. This gives a total gas flow of $H_2O:CO:CO_2:H_2:N_2$ = 50:2:8:27.5:12.5. The standard mass hourly space velocity (MHSV) used for testing was 75000 L h^{-1} kg^{-1}. In-line IR analysis was performed to measure CO conversion. Selectivity was determined by the methanol content within the knockout pots downstream of the reactors. Space and mass velocity variation tests were performed at 65 h time-on-line by altering the flow for each catalyst bed. Relative activities were calculated by altering the flow for each catalyst bed in order to achieve 75% CO conversion after 75 h time-on-line. The total system flow was maintained using the by-pass line.

Characterisation Methods

Powder X-ray diffraction (XRD).

Measurements were performed using a PANalytical X'pert Pro diffractometer with Ni filtered CuK_α radiation source operating at 40 kV and 40 mA. Patterns were recorded over the range of 10-80° 2θ using a step size of 0.016°. All patterns were matched using the ICDD database. An *in-situ* Anton Parr XRK900 cell (internal volume of ~0.5 L) was used to monitor the formation of metallic Cu during the reduction of the CuO/ZnO materials. A flow of 2% H_2/N_2 (60 ml min^{-1}) was passed through the sample

bed while the cell was heated to 225 °C (ambient to 125 °C ramp rate = 10 °C min^{-1}, 125-225 °C ramp rate = 2 °C min^{-1}). The sample was then cooled to room temperature and a 20-100° 2θ scan performed. Copper crystallite size was estimated from peak broadening analysis of the XRD pattern using Topas Academic[30], and the volume weighted column height (L_{vol}) was calculated based on the methodology of Balzar *et al.*[31].

X-ray fine edge spectroscopy (XAFS).

Cu and Zn K-edge XAFS studies were carried out on the B18 beamline at the Diamond Light Source, Didcot, UK. Measurements were performed using a QEXAFS set-up with a fast-scanning Si (111) double crystal monochromator. The time resolution of the spectra reported herein was 1 min/spectrum (k_{max} = 14), and on average three scans were acquired to improve the signal-to-noise ratio of the data. All *ex-situ* samples were diluted with cellulose and pressed into pellets to optimise the effective edge-step of the XAFS data and measured in transmission mode using ion chamber detectors. All transmission XAFS spectra were acquired concurrently with the appropriate reference foil (Cu or Zn) placed between I_t and I_{ref}.XAS data processing and EXAFS analysis were performed using IFEFFIT [32] with the Horae package[33] (Athena and Artemis). The amplitude reduction factor, s_0^2, was derived from EXAFS data analysis of a known Cu reference compound, namely tenorite (CuO). For the fitting of the local co-ordination geometry of georgeite and malachite, Jahn-Teller distorted Cu-O bond was difficult to observe due to thermal disorder and so were fixed in the model.

X-ray pair distribution analysis

Synchrotron X-ray pair distribution function (PDF) data were collected on the 11-ID-B beamline at the Advanced Photon Source at Argonne National Laboratory. Powder samples were packed into kapton capillaries with an internal diameter of 1 mm. Room temperature powder X-ray diffraction data were collected at a wavelength of 0.2114 Å using the Rapid Acquisition PDF method[34]. The scattering data ($0.5 \leq Q \leq 22$ $Å^{-1}$) was processed into PDF data using the program GudrunX[35].

Fourier transform infrared spectroscopy.

Analysis was carried out using a Jasco FT/IR 660 Plus spectrometer in transmission mode over a range of 400-4000 cm^{-1}. Catalysts were supported in a pressed KBr disk.

Raman spectroscopy.

Raman spectra were obtained using a Renishaw inVia spectrometer equipped with an argon ion laser (λ = 514 nm).

Thermal gravimetric analysis (TGA).

TGA measurements were performed using a SETARAM Labsys analyser with sample masses of *ca.* 20 mg heated at 1 °C min^{-1} under air with a flow rate of 20 ml min^{-1}.

Evolved gas analysis (EGA).

EGA experiments were performed using a Hiden CATLAB under the same conditions used in the TGA experiments.

Copper surface area analysis

Copper surface area analysis was determined by reactive frontal chromatography. Catalysts were crushed and sieved to a particle size of 0.6-1 mm and packed into a reactor tube. The catalyst was purged under helium for 2 min at 70 °C before being heated under a 5% H_2 reduction gas to 230 °C (8 °C min^{-1}) for 3 h. The catalyst was then cooled to 68 °C under helium prior to the addition of the dilute 2.5% N_2O reaction gas with a flow rate of 65 ml min^{-1}. The formation of N_2 from the surface oxidation of the copper catalyst by N_2O was measured downstream using a TCD. Once the surface of the copper was fully oxidised there would be a breakthrough of N_2O detected on the TCD. From this, the number of oxygen atoms chemisorbed on the copper surface could be determined. The number of exposed surface copper atoms and the copper surface area was subsequently derived from this analysis. Quoted surface areas are calculated using discharged sample mass. *Important note:* Recent work has shown that if the catalyst is exposed to partial pressures of hydrogen exceeding 0.05 bar then partial reduction of ZnO at Cu interface can occur. This will effect copper surface area results due to N_2O oxidising both Cu and ZnO_x. In these cases, alternative techniques, such as H_2 TPD will give more accurate data with respect to copper surface area.[36, 37]

LTS conditions copper surface area analysis

Copper surface area analysis of the fresh catalysts were carried out on a Quantachrome ChemBET 3000. 100 mg of sample was packed into a stainless steel U-tube and purged with high purity He for 5 minutes. Samples were reduced using 10% H_2/Ar (30 ml min^{-1}) heated to 140 °C at 10 °C/min, before heating further to 225 °C at 1 °C/min. The resulting catalyst was held at this temperature for 20 minutes to ensure complete reduction took place. It is important to note that under this partial pressure of H_2 it has been reported that ZnO species in contact with Cu can partially reduce. [36, 37] Residual H_2 was flushed from the system by switching the gas line back over to He (80 ml/min), whilst holding the sample at 220 °C for another 10 minutes. The temperature was then reduced down to 65 °C for N_2O pulsing (BOC AA Grade). A programme of 12 pulses of 113 µl N_2O with a 5 min. stabilisation time between pulses was carried out, followed by 3 pulses of N_2 for calibration. Unreacted N_2O was trapped before reaching the detector using a molecular sieve 5A (pelleted, 1.6 mm, Sigma Aldrich) trap. The Cu surface area was determined from the amount of N_2 emitted and the post analysis of catalyst mass (**Equation 1.**).

Equation 1. $$\text{Cu surface area } (m^2g^{-1}) = \frac{N_2 \text{ volume (ml)} \times N_A \times 2}{\text{catalyst mass (g)} \times 24000 \text{ (ml)} \times (1.47 \times 10^{19} \text{ (atoms/m}^2))}$$

whereby N_A = Avogadro constant = 6.022×10^{23} (atoms). The key assumptions are that the amount of N_2 emitted amounts to half a monolayer coverage of oxygen and that the surface density of Cu is 1.47×10^{19} (atoms/m^2). The volume of N_2 produced was quantified using a thermal conductivity detector (TCD).

After Cu surface area analysis, the samples were kept under N_2 and transferred to a LTS reactor. Ageing was carried out in a single fixed-bed reactor equipped with a by-pass line. CO, N_2, CO_2 and H_2 were introduced to the catalyst bed via mass-flow controllers (Bronkhorst). HPLC grade water was passed through a liquid-flow controller (Bronkhorst) and then into a controlled evaporator mixer (Bronkhorst) that was heated to 140 °C. N_2 was fed through the vapourised water to give a dilute syngas mixture (H_2O:CO:CO_2:H_2:N_2 = 25:1:4:13.75:56.25). This mixture was introduced at 220 °C after re-reduction of the catalyst. The gas flows were controlled to achieve a MHSV of 30,000 L h^{-1} kg^{-1}. After ageing for 40 h the samples were transferred back to the Quantachrome ChemBET Chemisorption analyser whereby after re-reduction the copper surface areas of the aged catalysts was measured, as described above.

Scanning Transmission Electron Microscopy

Samples for electron microscopy characterization were dry dispersed onto holey carbon TEM grids. They were examined in an aberration corrected JEOL ARM-200FS scanning transmission electron microscope operating at 200kV in BF- and DF-STEM imaging modes. Reliable electron microscopy results could only be obtained from the set of zincian georgeite and zincian malachite derived materials as these were found to be (i) stable under the vacuum environment of the microscope and (ii) largely unaffected by electron beam irradiation. By way of contrast, the Cu-only georgeite precursor materials were found to be highly unstable under vacuum conditions (even without electron beam irradiation) turning them from a blue to dark green colour, probably due to the loss of occluded water. The corresponding zincian georgeite materials showed no such colour transformation under vacuum.

Environmental Transmission Electron Microscopy

Samples for reduction during environmental transmission electron microscopy (ETEM) characterization were dry dispersed on heater chips (DensSolution trough hole) and then mounted on a DensSolution SH30 heating holder. The holder with sample was inserted into an FEI Titan 80-300 ETEM operated at 300kV.[38] The reduction of the samples was performed *in-situ* by the following procedure for both the georgeite and malachite precursors: A flow of H_2 was let into the ETEM building up a pressure of 2 mbar. The sample was heated from room temperature to 150°C using a heating ramp rate of 10°C/min. The final heating to 225°C was done at 1°C/min. The oxidation state of Cu was

monitored by Electron Energy-Loss Spectroscopy (EELS) during the reduction treatment using a Gatan Tridiem 866 spectrometer attached to the microscope. After an extended *in-situ* treatment of several hours at 225°C, HRTEM imaging was performed at elevated temperature in an H_2 atmosphere for both the georgeite and malachite samples using a Gatan US 1000 CCD camera.

X-Ray Photoelectron spectroscopy

A Kratos Axis Ultra DLD system was used to collect XPS spectra using monochromatic Al $K\alpha$ X-ray source operating at 120 W. Data was collected with pass energies of 160 eV for survey spectra, and 40 eV for the high resolution scans. The system was operated in the Hybrid mode, using a combination of magnetic immersion and electrostatic lenses and acquired over an area approximately 300 × 700 μm^2. A magnetically confined charge compensation system was used to minimize charging of the sample surface and the resulting spectra calibrated to the C(1s) line at 284.8 eV; all spectra were taken with a 90° take off angle. A base pressure of ~ 1×10^{-9} Torr was maintained during collection of the spectra. Gas treatments were performed in a Kratos catalysis cell which mimics the conditions of a normal reactor vessel allowing the recreation of reactor conditions and analysis of the chemical changes taking place on the surface of the catalyst. Briefly the cell consists of a fused quartz reactor vessel contained within a stainless steel vacuum chamber (base pressure ca. 10^{-8} Torr after baking). Samples were heated at a controlled ramp rate of 2 °C min^{-1} to at temperature of 225 °C using a eurotherm controller. The catalysts were exposed to an atmosphere of 2%H_2 in nitrogen with a flow rate of 30 ml min^{-1} controlled using MKS mass flow controllers, during the heating ramp, the 20 min isotherm at 225 °C and also while the catalyst was cooled to 25 °C. The samples were analysed before and after gas treatment without breaking vacuum.

ICP-MS and CHN analysis

ICP-MS and CHN were provided as commercial service by Warwick Analytical Services.

Helium pycnometry

Helium pycnometry was provided as a commercial service by MCA Services.

Additional references

30 Coelho, A. A., TOPAS Academic: General Profile and Structure Analysis Software for Powder Diffraction Data, Bruker AXS, Karlsruhe, Germany, (2010).

31 Balzar, D., Audebrand, N., Daymond, M. R., Fitch, A., Hewat, A., Langford, J. I., Le Bail, A., Louer, D., Masson, O., McCowan, C. N., Popa, N. C., Stephens, P. W. & Toby, B. H. Size-strain line-broadening analysis of the ceria round-robin sample. *J. Appl. Crystallog*r., **37**, 911-924, doi:10.1107/S0021889804022551 (2004).

32 Newville, M. IFEFFIT: interactive XAFS analysis and FEFF fitting. *J. Synchrot. Radiat.* **8**, 322-324, doi:10.1107/s0909049500016964 (2001).

33 Ravel, B. & Newville, M. ATHENA, ARTEMIS, HEPHAESTUS: data analysis for X-ray absorption spectroscopy using IFEFFIT. *J. Synchrot. Radiat.* **12**, 537-541, doi:10.1107/s0909049505012719 (2005).

34 Chupas, P. J., Qiu, X., Hanson, J. C., Lee, P. L., Grey, C. P. & Billinge, S. J. L. Rapid-acquisition pair distribution function (RA-PDF) analysis. *J. Appl. Crystallogr.* **36**, 1342-1347, doi:10.1107/S0021889803017564 (2003).

35 Soper, A. K. & Barney, E. R. Extracting the pair distribution function from white-beam X-ray total scattering data. *J. Appl. Cryst.* **44**, 714-726, doi:10.1107/S0021889811021455 (2011).

36 Fichtl, M. B., Schumann, J., Kasatkin, I., Jacobsen, N., Behrens, M., Schlögl, R., Muhler, M. & Hinrichsen, O., Counting of Oxygen Defects versus Metal Surface Sites in Methanol Synthesis Catalysts by Different Probe Molecules, *Angew. Chem. Int. Ed.* **53**, 7043-7047, doi:10.1002/anie.201400575, (2014)

37 Kuld, S., Conradsen, C., Moses, P. G., Chorkendorff, I., Sehested, J.,Quantification of Zinc Atoms in a Surface Alloy on Copper in an Industrial-Type Methanol Synthesis Catalyst, *Angew. Chem. Int. Ed.* **53**, 5941-5945, doi:10.1002/anie.201311073, (2014)

38 Hansen, T.W., Wagner, J. B., Dunin-Borkowski, R. E., Aberration corrected and monochromated environmental transmission electron microscopy: challenges and prospects for materials science, *Mater. Sci. Technol.,* **26**, 1338-1344, doi:10.1179/026708310X12756557336355, (2010)